AIAA Guidance, Navigation, and Control Conference and Exhibit
21 - 24 August 2006, Keystone, Colorado

AIAA 2006-6711

Estimation and Control of a Quadrotor Vehicle Using Monocular Vision and Moiré Patterns

Glenn P. Tournier*, Mario Valenti†, and Jonathan P. How‡
Massachusetts Institute of Technology, Cambridge, MA 02139

Eric Feron§
Georgia Institute of Technology, Atlanta, GA 30322

We present the vision-based estimation and control of a quadrotor vehicle using a single camera relative to a novel target that incorporates the use of moiré patterns. The objective is to acquire the six degree of freedom estimation that is essential for the operation of vehicles in close proximity to other craft and landing platforms. A target contains markers to determine its relative orientation and locate two sets of orthogonal moiré patterns at two different frequencies. A camera is mounted on the vehicle with the target in the field of view. An algorithm processes the images, extracting the attitude and position information of the camera relative to the target utilizing geometry and four single-point discrete Fourier transforms on the moiré patterns. The position and yaw estimations with accompanying control techniques have been implemented on a remote-controlled quadrotor. The flight tests conducted prove the system's feasibility as an option for precise relative navigation for indoor and outdoor operations.

I. Introduction

ACCURATE attitude and position information is critical for vehicles to perform their missions. In many cases, not only is accuracy important but the information is needed in real-time at the highest possible rate. Helicopters and quadrotors can hover, takeoff, and land in small locations enabling them to perform tasks fixed-wing craft are unable to perform. Landing rotorcraft unmanned aerial vehicles (UAVs) requires precise knowledge of the relative orientation and position of the UAV to the landing surface at higher rates than GPS can provide. GPS is also more susceptible to error near the ground or in cluttered environments. An inherent problem in landing is due to the difficulty in estimating the relative angle between the landing surface and the vehicle when the angle is small. This angle difference however can mean the difference between a successful touchdown and a damaged vehicle. The ability to control the craft decreases as it approaches the landing surface due to ground effect[1] increasing the need for a high rate, accurate 6 degree of freedom(DOF) relative positioning sensor.

A great deal of previous work has been conducted using vision for navigation. The vision algorithm using moiré pattern hypothesized by Feron et. al.[2] in one dimension is furthered here to multiple dimensions. Algorithms used to estimate vehicle attitude and/or position have included using vanishing points of parallel lines,[3] calculating locations or areas of colored blobs,[4,5] and extracting specific target feature points with known physical distances between them in images.[1,6] In other systems, vision is only used as a secondary sensor to GPS, requiring vehicle operation outdoors. A few of these methods have only been hypothesized or simulated, making it difficult to assess their effectiveness in actual flight conditions. Other methodologies use

*Student Member AIAA, S.M. Candidate, Department of Aeronautics and Astronautics, Massachusetts Institute of Technology, Cambridge, MA 02139 gpt20@mit.edu. Author to whom all correspondence should be addressed.

†Student Member AIAA, Ph.D. candidate, Department of Electrical Engineering and Computer Science, Massachusetts Institute of Technology, Cambridge, MA 02139 valenti@mit.edu

‡Associate Fellow AIAA, Associate Professor of Aeronautics and Astronautics, Autonomous Controls Laboratory, Massachusetts Institute of Technology, 77 Massachusetts Ave, M.I.T. Rm 33-326, Cambridge, MA 02139 jhow@mit.edu

§Associate Fellow AIAA, Professor of Aerospace Engineering, Georgia Institute of Technology, Atlanta, GA 30322 eric.feron@aerospace.gatech.edu

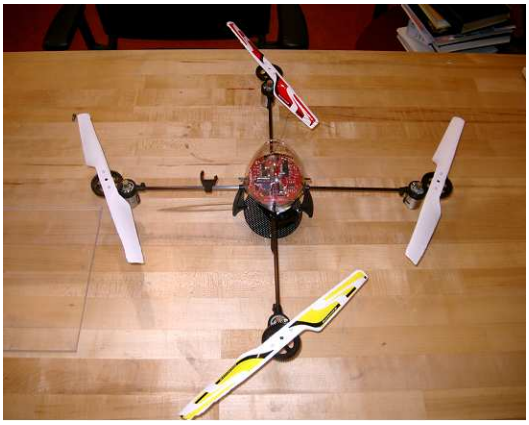

Figure 1. Quadrotor Vehicle.

cameras set up in stereo to determine vehicle position but increase the cost.[4,7] Commercially available indoor positioning systems such as those that use multiple camera vision,[8] lasers,[9] or GPS pseudo-constellations[10] can be also used to determine the 6 DOF of a vehicle. Although these systems perform well, the quantities of cameras or other sensors needed to locate the object make their use impractical as potential solutions in many environments such as landing on an aircraft or a moving truck.

We present a quadrotor system that flies autonomously given yaw and position data using a single onboard camera and a target in the field of view generating moiré patterns. An example quadrotor vehicle can be seen in Figure 1. The algorithms are computationally efficient as no least-squares estimations[6] or other complex mathematical computations need to be performed. Only a single camera, computation power, and inexpensive custom target are required. The system also enables operation in both enclosed areas and outdoors.

This paper begins with a general description of the moiré target in Section II. We then discuss how position and attitude are computed in Section III. Algorithm flow is described in Section IV and Section V gives a description of the system and associated controllers. Results of calibrated tests and flight tests are given in Section VI.

II. Moiré Target Overview

Moiré patterns can be generated in a variety of ways, including superimposing one semitransparent grating above another, either at an angle, using different grating sizes, or placing them a set distance apart. The target used here generates the patterns by the latter method. The attractive feature of moiré patterns generated in this fashion is their ability to amplify movement. What could be considered a slight movement of the gratings or a camera as compared to the grid size, is visually seen as much larger in the moiré pattern. For the control of a quadrotor, the primary interest is tracking the effect of camera movement. If the camera translates in any direction, it appears as if the moiré patterns "move" inside the target in the same direction the camera moved, giving an indication of position change. However, if the camera rotates in any way, the patterns do not "move" within the target.

Another characteristic of the patterns is that their apparent wavelength on the image plane remains nearly constant at all altitudes assuming small rotations. As height increases, the wavelength of the patterns with respect to the target increases, i.e. fewer patterns appear within the target. This effect is exactly canceled by the fact that an object gets smaller on an image plane as the distance between it and the camera increases. This cancelation results in a near constant apparent wavelength on the image plane. Understanding these fundamental principles allow accurate position and attitude information to be obtained from the moiré patterns.

The interference effect is generated by having two identical sets of gratings placed in parallel with one

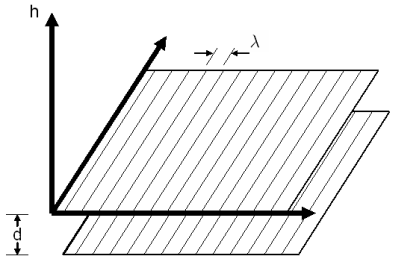

Figure 2. Gratings to generate moiré patterns.

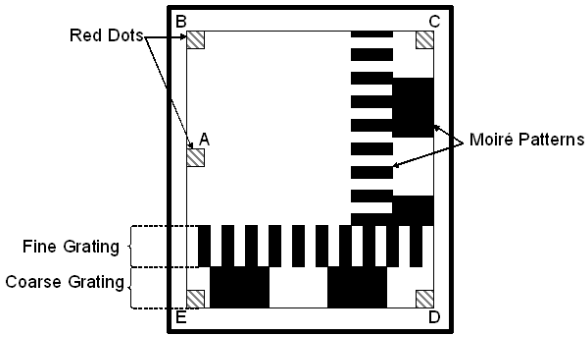

Figure 3. Moiré target with key features labeled.

on of top of the other a distance d apart as shown in Figure 2. The gratings in the figure are regularly spaced with characteristic wavelength λ. The printed gratings are referred to as Ronchi rulings where the transmittance profile is a square wave which is opaque for exactly half of the duty cycle and transparent for the remaining half.[11]

Figure 3 shows a drawing of the target with key features labeled including the moiré patterns created by the gratings. The actual target as it appears on the image plane of the camera is shown in Figure 4. Five red lights on the target are used as feature points with the off-corner red light used to determine the orientation of the target. The red lights are given a reference letter as seen in Figure 3.

Referred to as the red dots on the image plane, the red lights are used to find the coarse and fine gratings and compute yaw and altitude. Identical grating sets are printed in orthogonal directions. The difference between the fine gratings and coarse gratings is their characteristic wavelength λ shown in Figure 2. The coarse grating wavelength is larger than that of the fine grating, generating a lower frequency moiré pattern. The purpose of the different moiré pattern wavelengths will be discussed later.

III. Pose Estimation Equations

In this section, we present how the target allows the system to calculate the 6 DOF of the camera using moiré patterns and geometry. The altitude and yaw estimations rely entirely on geometry while the lateral translations and rotations about those axes incorporate the use of the patterns.

The several coordinate systems used to perform the calculations are shown in Figure 5. A fixed inertial frame (X, Y, Z) is assumed to be connected to the target with the origin located on the red light labeled B. A vehicle coordinate system is connected through its center of mass (x_v, y_v, z_v) and another set is connected through the camera, (x_c, y_c, z_c) with the origin at the focal point, F. The image plane is described by (u, v). Pitch, roll, and yaw are all given in the camera coordinate system as Θ, Φ, and Ψ respectively.

A. Position

A pinhole model of the camera is assumed to calculate the altitude of the vehicle relative to the target, and we assume that the camera is located at the vehicle's center of gravity, i.e. the vehicle coordinate system is

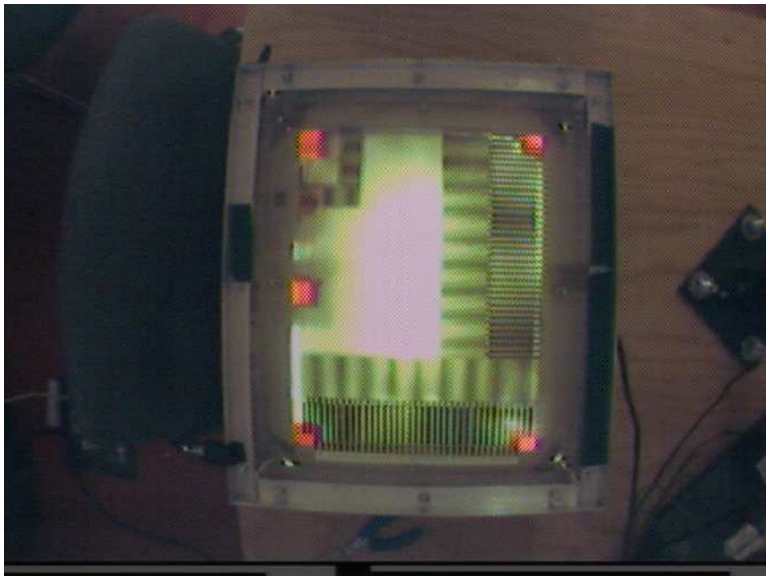

Figure 4. Actual image of moiré target as seen by the camera.

identical to the camera coordinate system. In addition, the image plane is assumed to be nearly parallel to the target plane when the camera is looking down at the target such as during a hover or landing condition. Given these assumptions, the basic principle of similar triangles can be applied as shown in Figure 6 to compute altitude. F is the focal point of the camera, P is the principle point, K is the point is directly below, and D and E are points on the target in the fixed coordinate frame (X, Y, Z) while D' and E' are the equivalent points as they appear in the image plane (u, v). The principle point is defined as the point where the line that is perpendicular to image plane goes through the focal point and intersects the image plane. Since $\triangle FKD$ is similar to $\triangle FPD'$ and $\triangle FKE$ is similar to $\triangle FPE'$, we obtain the altitude, h, using

$$\frac{s}{h} = \frac{r}{f}. \tag{1}$$

The calculation requires knowledge of the physical distance between the feature points on the target, s, the corresponding distance in the image in pixels, r, and the focal length of the camera, f, in units of pixels. The altitude is computed four times using the lines $\overline{BC}$, $\overline{CD}$, $\overline{ED}$, and $\overline{EB}$ on the image. The resulting values are averaged to remove the effect of perspective. This is an appropriate method given the assumption of nearly parallel image and target planes.

Since the top and bottom gratings are printed in one dimension, the analysis will assume a one-dimensional problem focusing on two gratings. Each grating is represented as a square wave with a Fourier transform of

$$\mathcal{F}\{f(y)\} = \sum_{i=-\infty}^{\infty} \frac{\sin\frac{\pi i}{2}}{\pi i}\delta\left(f - \frac{i}{\lambda}\right) \tag{2}$$

consisting of impulses at integer multiple frequencies of the printed pattern. Given that the magnitude of the sine components decays inversely with frequency, a first order raised cosine model, $i = 0, \pm 1$ in Equation 2, can be used to approximate the square wave.

Modeling of the printed gratings using raised cosine function approximations to the square wave can be seen in Figure 7. The figure represents the view from the side of the two superimposed gratings of the printed wavelength λ at a distance apart d. We let the origin be the start of the gratings, x be the distance to the camera focal point, y be the distance to the ray of light entering the camera from the top grating, and h be the altitude, i.e. the distance between the focal point and target surface. The angle between the vertical and the ray of light of interest is γ. Using these variables, the top and bottom pattern are modeled as

$$f_{\mathcal{T}}(y) = \frac{1}{2} + \frac{1}{2}\cos\left(\frac{2\pi}{k\lambda}y\right) \tag{3}$$

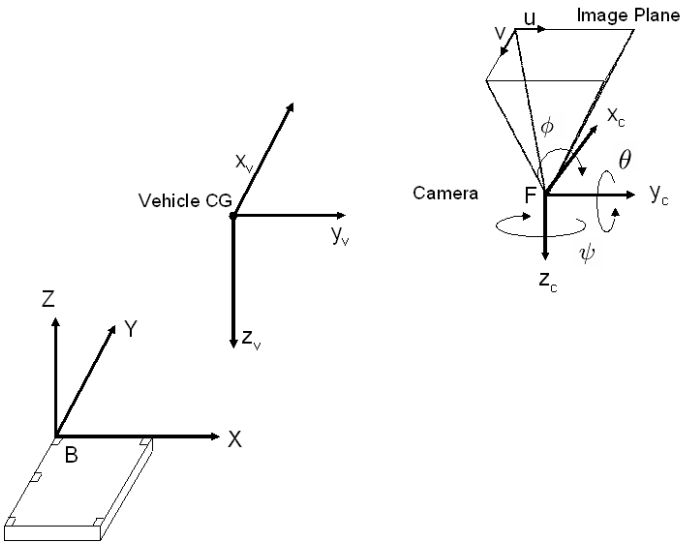

Figure 5. Coordinate Systems.

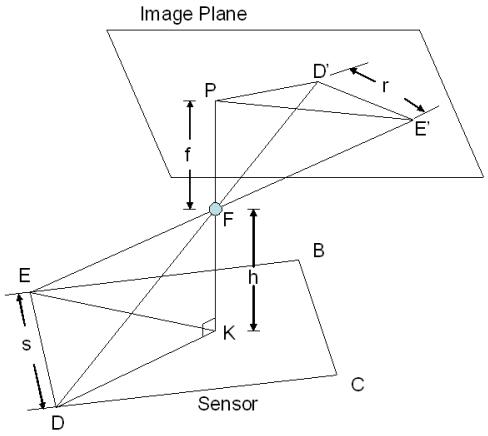

Figure 6. Calculation of altitude.

$$f_{\mathcal{B}}(y) = \frac{1}{2} + \frac{1}{2}\cos\left(\frac{2\pi}{k\lambda}(y - d\tan\gamma) + \psi\right). \tag{4}$$

The phase offset ψ accounts for lateral misalignment error of the gratings when placed one over the other. The k variable corrects for the refraction of light as it passes through the transparent acrylic sheets that sandwich the printed grating sheets to hold them in place. The physical layout of the target will be described further in Section V.

The overall intensity of the observed moiré pattern, $\mathcal{I}$, is computed through the multiplication of the equations of the individual grating intensities:

$$\mathcal{I} = \left[\frac{1}{2} + \frac{1}{2}\cos\left(\frac{2\pi}{k\lambda}y\right)\right]\left[\frac{1}{2} + \frac{1}{2}\cos\left(\frac{2\pi}{k\lambda}(y - d\tan\gamma) + \psi\right)\right]. \tag{5}$$

The following equations exist due to the geometry of the problem and from a trigonometric identity:

$$\tan\gamma = \frac{x - y}{h}, \tag{6}$$

$$\left(\frac{1}{2} + \frac{1}{2}\cos a\right)\left(\frac{1}{2} + \frac{1}{2}\cos b\right) = \frac{1}{4} + \frac{1}{4}\cos a + \frac{1}{4}\cos b + \frac{1}{8}\cos(a+b) + \frac{1}{8}\cos(a-b). \tag{7}$$

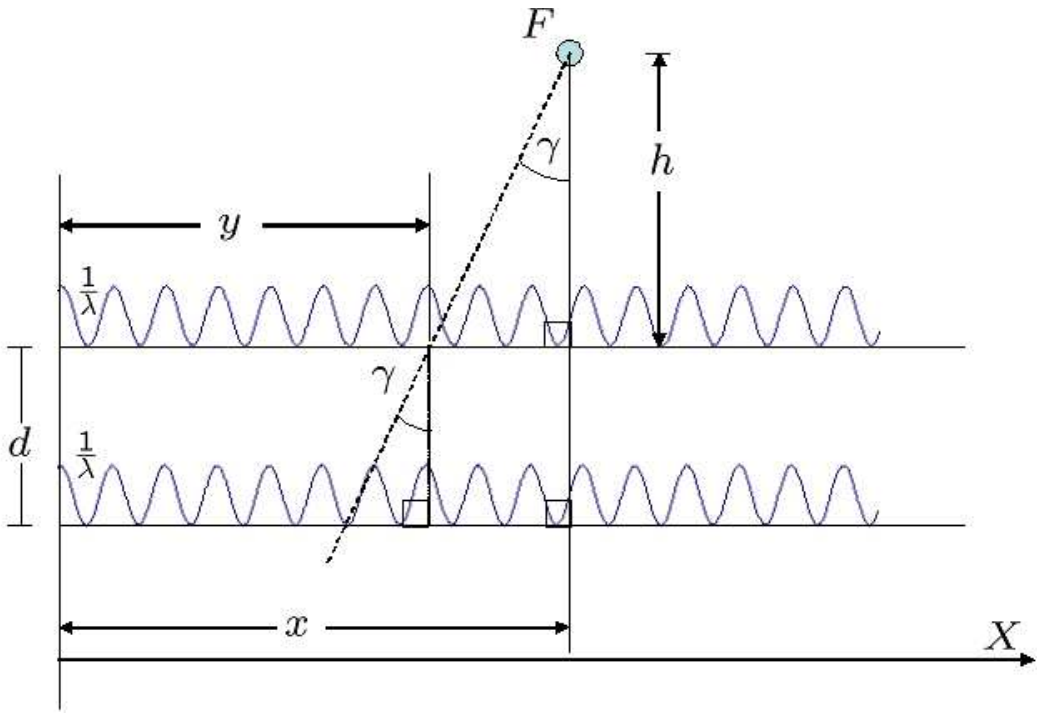

Figure 7. Target and camera as seen from the side with grating intensity represented by a cosine function.

Combining them with overall Equation 5 creates

$$\mathcal{I} = \frac{1}{4} + \frac{1}{4}\cos\left(\frac{2\pi}{k\lambda}y\right) + \frac{1}{4}\cos\left(\frac{2\pi d}{hk\lambda}\left(\left(\frac{h}{d}-1\right)y - x\right) + \psi\right) + \\ + \frac{1}{8}\cos\left(\frac{4\pi y}{k\lambda} - \frac{2\pi d}{hk\lambda}(x-y) + \psi\right) + \frac{1}{8}\cos\left(\frac{2\pi d}{hk\lambda}(x-y) - \psi\right). \tag{8}$$

The first three terms in the equation are the functions of the original gratings. The final two terms enter from the convolution of the gratings in the frequency domain and represent the moiré patterns. The last term is the lower frequency difference term and the second-to-last is the higher frequency sum term. The primary objective is to track the phase of the low frequency moiré term since the high frequency moiré term is filtered out by the camera.

To calculate the position of the camera relative to the target, a single-point discrete Fourier transform (DFT) at both known apparent frequencies on the image plane is performed along each grating in the direction of the grating seen in Figure 8. The input values to the DFT are the summation of the red-green-blue (RGB) values of each pixel starting at the origin. The independent variable over which the DFT is computed is y, given it represents the location of the source of the ray of light entering the camera generating each pixel's RGB values. Therefore, the phase of the visible pattern corresponding to the lowest prominent frequency is

$$\phi = \frac{2\pi d}{hk\lambda}x - \psi \tag{9}$$

as given in the last term of Equation 8.

We see in Equation 9 that as the camera moves, the phase measured at the beginning of the gratings (or any other constant point on the target) changes, indicating the pattern is "moving" within the target. We have chosen the DFT to always be performed at the start of the gratings on the target, regardless of where the target lies in the image. When performing the calculations, we must remember that phase is subject to integer wrapping of 2π. The number of integer wraps in both x and y in moving the camera from its current location to above the origin of the inertial set of coordinates must be correctly determined by the

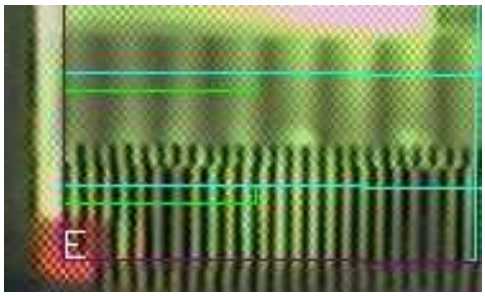

Figure 8. The target with a Discrete Fourier Transform (DFT) computed along the line in the direction of the gratings.

algorithm to accurately calculate the position. The position of the camera relative to the beginning of the grating incorporating the 2π wrapping of the phase and solving for x in Equation 9 gives

$$x = \frac{hk\lambda}{2\pi d}(\phi - 2\pi n + \psi). \tag{10}$$

Phase unwrapping introduces complexity to the system. Issues occur when the camera is moving with enough velocity so the phase difference of the fine pattern between consecutive frames is greater than π if unwrapped correctly. In this case, the system cannot determine whether to increase, decrease, or maintain the wrapped phase by an integer amount of 2π and the position cannot be recovered without additional computation. The fine grating measurement is most susceptible to this error since it requires a smaller amount of movement to incur a 2π wrap. The purpose of the coarse set of gratings is to assist in solving this problem. By having a longer wavelength, it takes a larger movement between frames (corresponding to a higher camera velocity) for it to lose track of its correct value of n. The compromise for this higher tolerance for high velocities is a decrease in accuracy as the distance moved per degree is lower at these longer wavelengths. However, the better accuracy of the fine grating can still be used when compared to the rough position calculation provided by the coarse gratings. If the difference between the coarse grating position and fine grating position is less than the distance corresponding to a phase shift of π of the fine gratings, phase unwrapping is considered successful and the fine grating position is assumed to be correct. The algorithm then moves on to the next frame. However, if the distance is larger than that distance corresponding to a phase shift of π of the fine gratings, the fine grating phase is assumed to have unwrapped incorrectly and is giving an inaccurate location. The coarse grating position is then used in Equation 10 with the fine grating phase information to calculate the most probable value of n and round it to the nearest integer. The position calculation is then recomputed using that value of n.

Equation 10 calculates position from the start of the fringes given altitude and the proper integer value of n. The same equation is employed using the computed phase of the orthogonal set of fringes on the target, thus the 3D location of the camera in the inertial frame is known.

B. Attitude

Although pitch, Θ, and roll, Φ, are not currently utilized in the system, the vision target provides the three attitude angles of the camera in addition to its location. The computation of attitude is similar to that of position but instead of requiring the DFT to always begin where the gratings start on the actual target in the image, the pitch and roll calculations require the DFT be performed on the same point on the image plane regardless of where the gratings start.

Figure 9 shows a variation on the approach to viewing the target and camera from the side. Assuming similar cosine intensity equations to Equation 3 and Equation 4 with y_t and y_b representing the distance from the origin to the light rays, the product of the equations is

$$\mathcal{I} = \left[\frac{1}{2} + \frac{1}{2}\cos\left(\frac{2\pi y_t}{k\lambda}\right)\right] \left[\frac{1}{2} + \frac{1}{2}\cos\left(\frac{2\pi y_b}{k\lambda} + \psi\right)\right], \tag{11}$$

giving the overall intensity of the observable fringes in the coordinate system of Figure 9. The geometry of

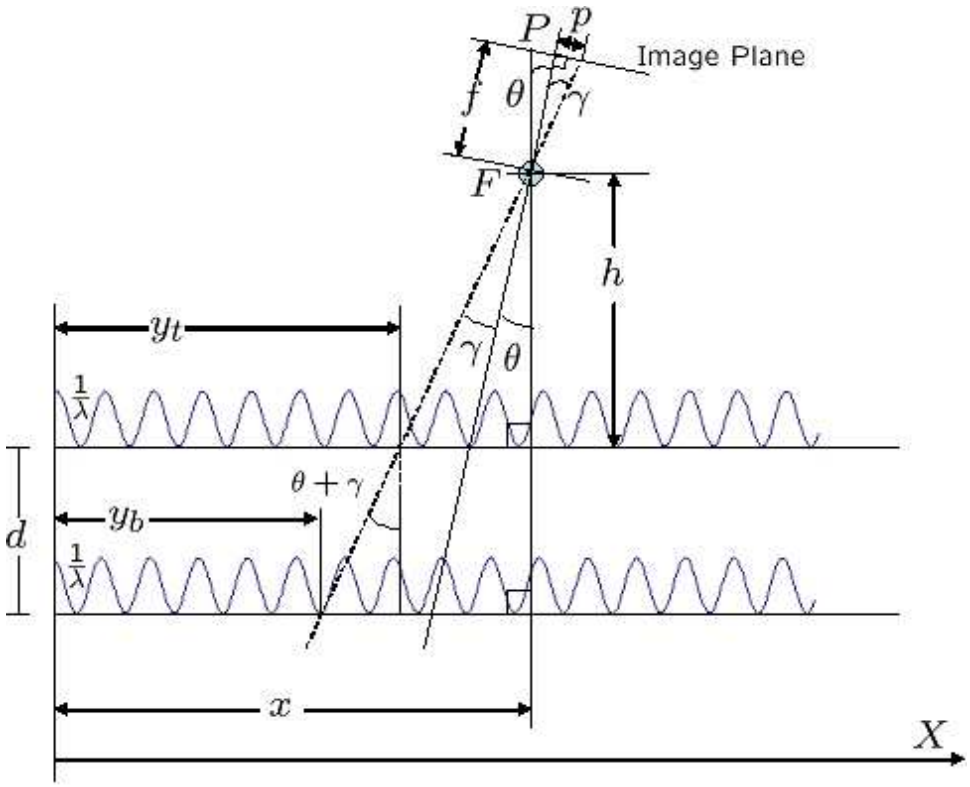

Figure 9. A different approach to the viewing the target and camera as seen from the side with grating intensity represented by a cos **function.**

the problem is

$$\tan(\theta+\gamma) = \frac{x-y_b}{h+d} = \frac{y_t-y_b}{d} \tag{12}$$

$$\tan\gamma = \frac{p}{f} \tag{13}$$

where γ is the angle from the vertical line running through the principle point, P, to the source of the light ray of interest where it hits the image plane a distance p from the principle point in Figure 9. Combining these equations with trigonometric identities gives the overall intensity equation

$$\begin{aligned}\mathcal{I} = \frac{1}{4} + \frac{1}{4}\cos\left(\frac{2\pi y_t}{k\lambda}\right) + \frac{1}{4}\cos\left(\frac{2\pi y_b}{k\lambda}+\psi\right) + \\ + \frac{1}{8}\cos\left(\frac{2\pi}{k\lambda}(y_t+y_b)+\psi\right) + \frac{1}{8}\cos\left(\frac{2\pi d}{k\lambda}\tan\left(\theta+\tan^{-1}\frac{p}{f}\right)-\psi\right).\end{aligned} \tag{14}$$

Looking at the lower frequency second term, the independent variable over which the intensity changes on the image plane is p. By setting p to 0, the remaining terms represent the phase at the principle point. Denoting the phase at that location ϕ_p, accounting for the 2π phase unwrapping, and solving for θ, the camera angle is

$$\theta = \tan^{-1}\left(\frac{k\lambda}{2\pi d}(\phi_p+\psi)\right). \tag{15}$$

Since the principle point is a known location on the image plane, the roll angle can be determined by always computing a DFT originating from P. However, this additional DFT does not need to be performed since the phase on the cosine wave is already known at the point where the gratings start, $x = 0$. Also, if P were to ever not lie in the plane of the target on the image, i.e. $x < 0$ or x greater than the size of the target when the image plane is parallel to the target plane, there would be no direct way to compute the phase since there would be no target generated fringes at P to do the DFT.

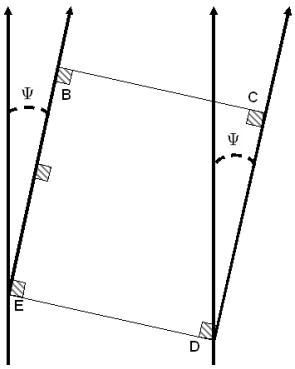

Figure 10. Yaw angle Ψ is determined by observing how parallel the lines $\overline{EB}$ and $\overline{DC}$ are to the vertical.

Given that the apparent wavelength, ρ, of the gratings remains nearly constant on the image plane as discussed previously, the phase at the principle point can be computed by first finding the perpendicular distance between P and the line where the gratings start in pixels, x_g. Given x_g and the known phase angle at the start of the gratings, the phase at the principle point, ϕ_p, is solved by

$$\phi_p = \frac{2\pi}{\rho} x_g + \phi - 2\pi n. \tag{16}$$

Equation 15 is then used to compute the attitude angle. Similar to the position computation, the same equation holds for the orthogonal set of fringes to calculate the angle about the other non-vertical axis.

Camera yaw, Ψ, is evaluated by observing how parallel the lines between feature points on the target are to the vertical. Using the red dots on the target, this implies

$$\Psi = \tan^{-1}\left(\frac{B_v - E_v}{B_u - E_u}\right) \tag{17}$$

as seen in Figure 10.

Since the target provides information for the exercise of landing, instances when the target is a great lateral distance away and the effect of perspective is prominent are outside the scope of the purpose of the target. Therefore, it was not necessary to include perspective in Equation 17. To minimize any small effect, the yaw angle is averaged between the angles returned by using $\overline{EB}$ and $\overline{DC}$.

IV. Algorithm

To extract all the information the target provides, the algorithm first captures an image and goes over each pixel. It removes the distortion introduced by the camera, finds the red dots, determines the target's orientation, finds the beginning of the gratings, knows the direction in which to acquire the data for the DFT, performs the DFT, unwraps the phase, and computes the 6 DOF of the camera relative to the target. The algorithm then repeats the process on the next captured frame. A flowchart of the algorithm can be found in Figure 11.

V. Integrated Vehicle System

To demonstrate the capabilities of this device in a real-time environment, we used this vision sensor technology to provide real-time positioning data for a Draganflyer V Ti Pro[12] (as shown in Figure 1) in an low-cost, indoor testing environment. The quadrotor is a four rotor helicopter that receives 4 input commands, one to each rotor. Two of the four rotors are counter-rotating to enable 6 degree of freedom movement. A wireless CMOS camera is attached to the vehicle pointing downward at the moiré target. Figure 12 shows a diagram of the components and setup of the integrated system. Notice that all of the computing for this system is done on a ground-based computer, which had two AMD 64-bit Operton processors, 2 Gb of memory, and ran Gentoo Linux. To command the vehicle, a circuit board was constructed

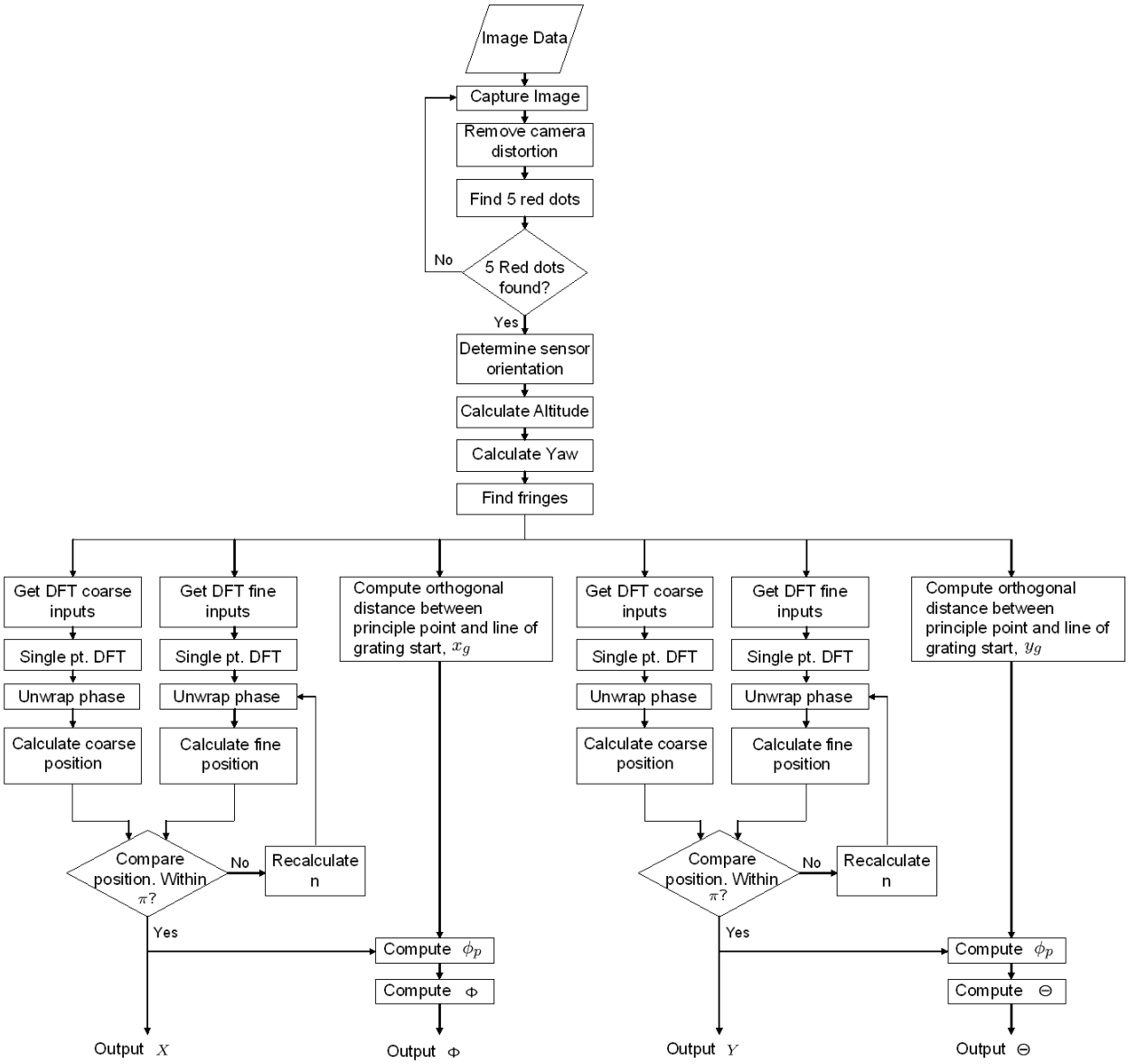

Figure 11. Vision algorithm flow chart computing the 6 DOF for a single frame.

to convert commands sent from the computer to the vehicle's transmitter via the trainer port interface. Thus, no modifications to the Draganflyer V Ti Pro on-board electronics were made for testing.

To detect the vehicle's position and orientation, two sensors were used. First, the MicroStrain 3DM-GX1 inertial navigation measuring device was used to detect the vehicle's pitch and roll rates. This data is preprocessed and filtered before becoming available for use by the control program. Second, the vision system (as described above) was used to detect the vehicle's heading, X, Y, and Z position. Note that picture of the target captured by the wireless camera is sent to a receiver which is connected to a LifeView FlyVideo 3000 FM capture card in the ground computer via a video cable. The camera data processed by the capture card is stored in a buffer for the vision sensor algorithm to process.

The moiré target was custom built at the Massachusetts Institute of Technology. The gratings were made by printing black lines on two transparencies using a laser-jet printer and placing each transparency between two sheets of acrylic. The two sheets were bolted together to hold the transparency in place and constitute a layer. Standoffs were used to maintain equal distance between two layers. To amplify the visibility of the moiré pattern, incandescent light bulbs were used as backlights. Special consideration was taken to ensure the lighting did not cause white-out of the camera image and to ensure the dots appeared red enough to be discerned from background red by the algorithm. The camera was calibrated to extract the location of its

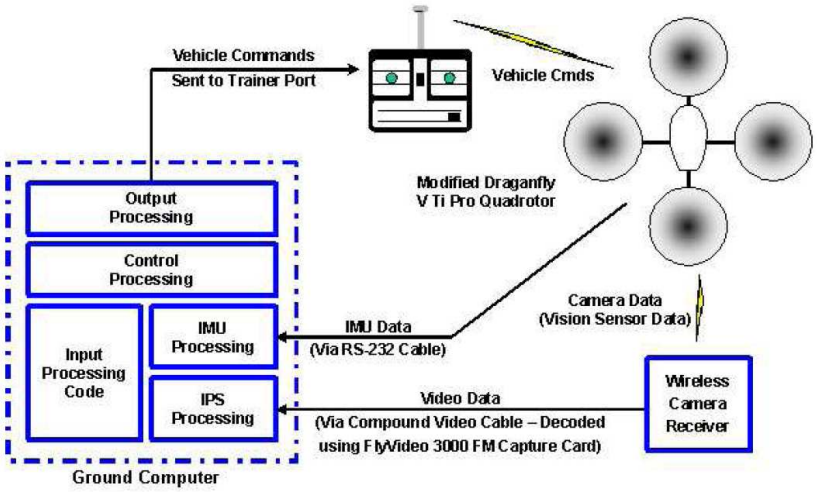

Figure 12. Integrated Vehicle System Block Diagram

principle point, its effective focal length, and its tangential and radial distortion coefficients. The images were digitally captured at a resolution of 640x480. The vision algorithm utilizes Intel's OpenCV,[a] a computer vision library, to remove distortion and access image pixel information to perform the computations.

From timing experiments, we found that there is a 50-100 ms delay between when the picture is taken by the camera and when the position data is available to the controller. Due to this latency and the limit in vision data rates in video capture and processing, pitch and roll data from the target were not used to control the vehicle. However, such data, when implemented on a dedicated processing platform to increase its frequency, could provide highly accurate position information necessary to supplement other sensors and possibly eliminate the need for an inertial measurement unit(IMU).

Next, a vehicle model was needed in order to control the vehicle via the computer. The coordinate system used in the model is the vehicle axes seen in Figure 5, which is rotated to that of the inertial coordinate system. Using a generic quadrotor vehicle model,[13] we have

$$
\begin{aligned}
\ddot{x} &= (\cos\phi\ \sin\theta\ \cos\psi\ +\ \sin\phi\ \sin\psi\ )\ \frac{1}{m}U_1 \\
\ddot{y} &= (\cos\phi\ \sin\theta\ \sin\psi\ -\ \sin\phi\ \cos\psi\ )\ \frac{1}{m}U_1 \\
\ddot{z} &= -g\ +\ (\cos\phi\ \cos\theta\ )\ \frac{1}{m}U_1 \\
\ddot{\phi} &= \dot{\theta}\,\dot{\psi}\left(\frac{I_y\ -\ I_z}{I_x}\right)\ -\ \frac{J_R}{I_x}\,\dot{\theta}\,d\ +\ \frac{L}{I_x}U_2 \\
\ddot{\theta} &= \dot{\phi}\,\dot{\psi}\left(\frac{I_z\ -\ I_x}{I_y}\right)\ +\ \frac{J_R}{I_y}\,\dot{\phi}\,d\ +\ \frac{L}{I_y}U_3 \\
\ddot{\psi} &= \dot{\phi}\,\dot{\theta}\left(\frac{I_x\ -\ I_y}{I_z}\right)\ +\ \frac{1}{I_z}U_4
\end{aligned}
$$

where x, y, z are the vehicle's position variables, ϕ, θ, and ψ are the roll, pitch and yaw orientations of the vehicle (respectively), I_x, I_y, and I_z are the body moment of inertias, L is the length between the vehicle center of gravity and a motor, m is the mass of the vehicle, g is the gravitational constant, J_R is the moment of inertia of a rotor blade, Ω represents a disturbance generated by differences in rotor speed, and U_1, U_2, U_3, and U_4 are the collective, roll, pitch and yaw input commands (respectively) for the vehicle. The linearized

[a]For more information: http://www.intel.com/technology/computing/opencv/index.htm

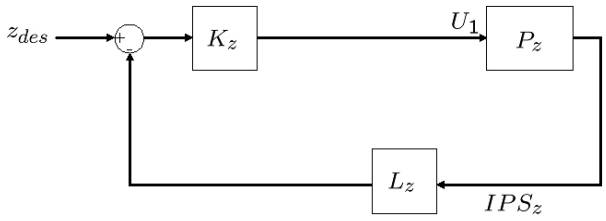

Figure 13. Block Diagram of the z-Position Control Loop.

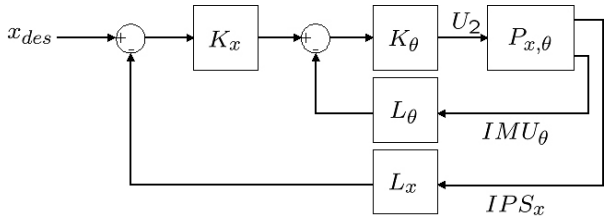

Figure 14. Block Diagram of the x-θ Control Loop.

model is

$$\begin{aligned}
\ddot{x} &= \theta \frac{1}{m} U_1 \\
\ddot{y} &= -\phi \frac{1}{m} U_1 \\
\ddot{z} &= -g + \frac{1}{m} U_1 \\
\ddot{\phi} &= \frac{L}{I_x} U_2 \\
\ddot{\theta} &= \frac{L}{I_y} U_3 \\
\ddot{\psi} &= \frac{1}{I_z} U_4
\end{aligned}$$

and let $U_1 = m\ g + \delta u_1$,

$$\begin{aligned}
\ddot{x} &= g\ \theta \\
\ddot{y} &= -g\ \phi \\
\ddot{z} &= \frac{1}{m} \delta u_1 \\
\ddot{\phi} &= \frac{L}{I_x} U_2 \\
\ddot{\theta} &= \frac{L}{I_y} U_3 \\
\ddot{\psi} &= \frac{1}{I_z} U_4
\end{aligned}$$

which is the simplified linearized vehicle model.

The controller architecture was broken into four groups: the x-θ, y-ϕ, z and ψ. To control the z position, an estimator was used to calculate the actual x location of the vehicle given the processed position data (as represented by L_z in Figure 13). Then, a PID controller was used to direct the vehicle to the desired

altitude. Note that a similar loop was used to maintain vehicle heading, ψ, during flight. Next, to control x position and θ angle, an estimator was used to calculate the actual x location of the vehicle given the processed position data as represented by L_x in Figure 14. Likewise, the pitch data from IMU was also filtered (to reduce the noise caused by mechanical vibrations). Then, two lead controllers (represented by K_x and K_θ respectively) were used to generate the appropriate pitch command to maintain the vehicle's position over the sensor during flight. Note that the y-ϕ loop was nearly identical to the x-θ loop because of vehicle's symmetry. The fine details of the controller have been omitted here given their standard use in various control problems.

VI. Results

The algorithms and controllers discussed previously were implemented on the quadrotor vehicle. The first set of experiments we conducted verified the accuracy of the moiré target. These tests were performed by putting the target in the field of view of the camera and manually moving it in the 6 DOF. A ground truth estimate of attitude and position was provided by an external positioning system while the computer was simultaneously running the vision algorithm. System performance is summarized into three altitude ranges which are further broken into two ranges of pitch and roll, high and low angle. The accuracy metric is the error variances which are specific for the camera and target as described here. Performance will vary using a different camera and/or target. The results of the tests performed and vertical operating range are given in Table 1.

Table 1. Summary of moiré target system maximum error variance using the camera and constructed target at three altitude ranges and two rotation angle ranges. Maximum and minimum altitude values based on Ψ are also given. Units in cm and degrees.

		Attitude: ±5 deg at Z			**Attitude: ±30 deg at Z**		
	Symbol	*28-51 cm*	*51-66 cm*	*66-90 cm*	*28-51 cm*	*51-66 cm*	*66-90 cm*
Altitude	Z	2.19	3.37	5.26	2.43	4.22	7.10
Translation	X	0.69	0.58	0.65	1.17	1.40	1.31
Translation	Y	0.34	0.42	0.54	0.66	0.87	0.76
Yaw	Ψ	0.94	1.55	1.22	3.59	2.52	0.97
Roll	Φ	1.53	0.51	0.27	1.39	1.77	1.20
Pitch	Θ	0.62	0.88	0.75	0.57	0.65	0.59

	Max (cm)	Min (cm), $\Psi = \pm 90$	Min (cm), $\Psi = 0$
Z	90.17	27.94	36.83

The error variance of the altitude measurement increases with height. This trend is an effect of the pixellation of the image. At higher altitudes, the target and red dots are represented by fewer pixels so any increase in measured pixel distance due to noise has a more prominent effect than a single pixel error at a lower altitude. This is most easily seen in the inverse relationship between the computed height and the pixel distance measurement seen in Equation 1. The altitude error is larger at higher attitude angles as well since the assumption of the camera plane being parallel to the target breaks down further in this regime. Although altitude error diminishes with the lowering of Z, the phase measurement error becomes more prevalent as the fringes themselves are increasing in resolution and become more susceptible to pixellation noise. Thus, the error variance for the translational directions at the different altitudes is nearly constant for each attitude. The increased error of Z at higher attitudes generates the larger translational errors at higher attitudes.

The yaw variance error decreases with increasing Z because the target begins to occupy fewer pixels of the screen. The non-uniformity of the "redness" of each of the red dots is more readily apparent when the camera is closer to the target giving small offsets between the centers of E, B, C, and D making the measurement more noisy. The roll and pitch error do not vary with height; they are functions of computed phase which

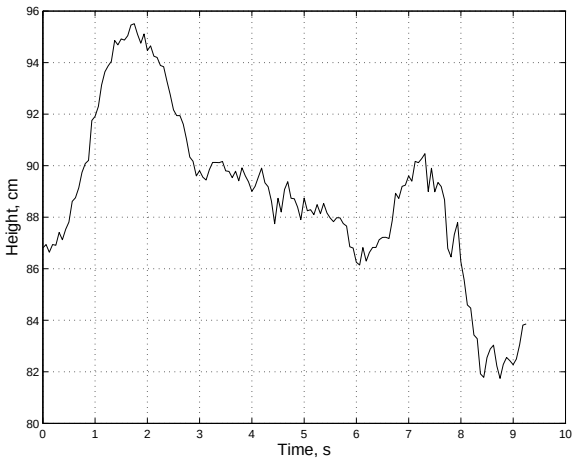

(a) Height

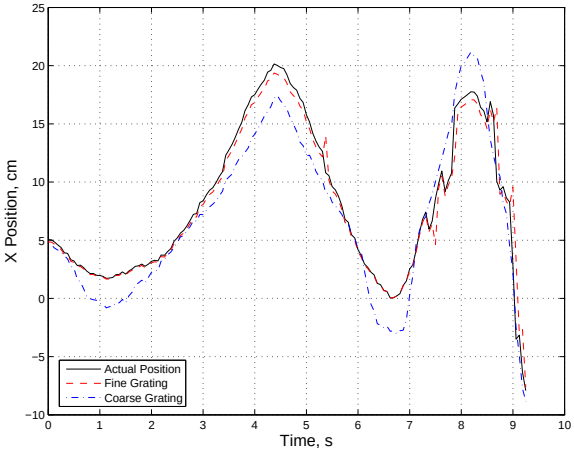

(b) X Position

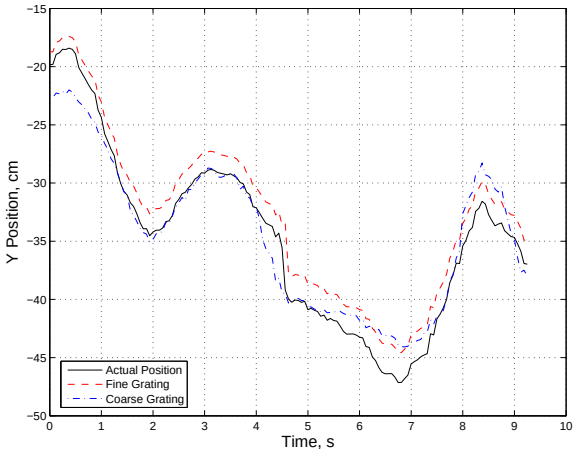

(c) Y Position

Figure 15. Position flight data for quadrotor in hover condition.

is subject to increased error when altitude decreases as described previously but are also functions of the accuracy of x_p, which becomes more accurate as resolution increases with the camera approaching the target thus complementing the effect of phase noise.[b]

Hover tests were performed to demonstrate the usability of the system to autonomously control the vehicle. The quadrotor was held above the target in the field of view of the camera and released. Figure 15 and Figure 16 show the results of a section of flight data when the target was used in an autonomous hover.[c] The X and Y positional plots contain the output position as well as the fine and coarse grating positions. From the figures, one can see the blending of positional information with high slopes on the fine grating position estimate. The figures demonstrate the ability of the quadrotor to remain hovered above the target for a sustained period of time. Latency in the position information in feedback loop and filtering of the velocity computation causes delayed responses of the vehicle to movement. This group delay then induces positional oscillations. Figure 16 shows the computed attitude of the vehicle during the flight. We see in the figure the ability of the system to determine relative orientation to the target. Although pitch and roll provided by the moiré target are not utilized by the current system, this information can be of great value for landing operations.

[b] A more detailed analysis of system performance can be found in the thesis by Tournier.[14]

[c] Video of quadrotor in hover operation can be found at `http://web.mit.edu/gpt20/www/`

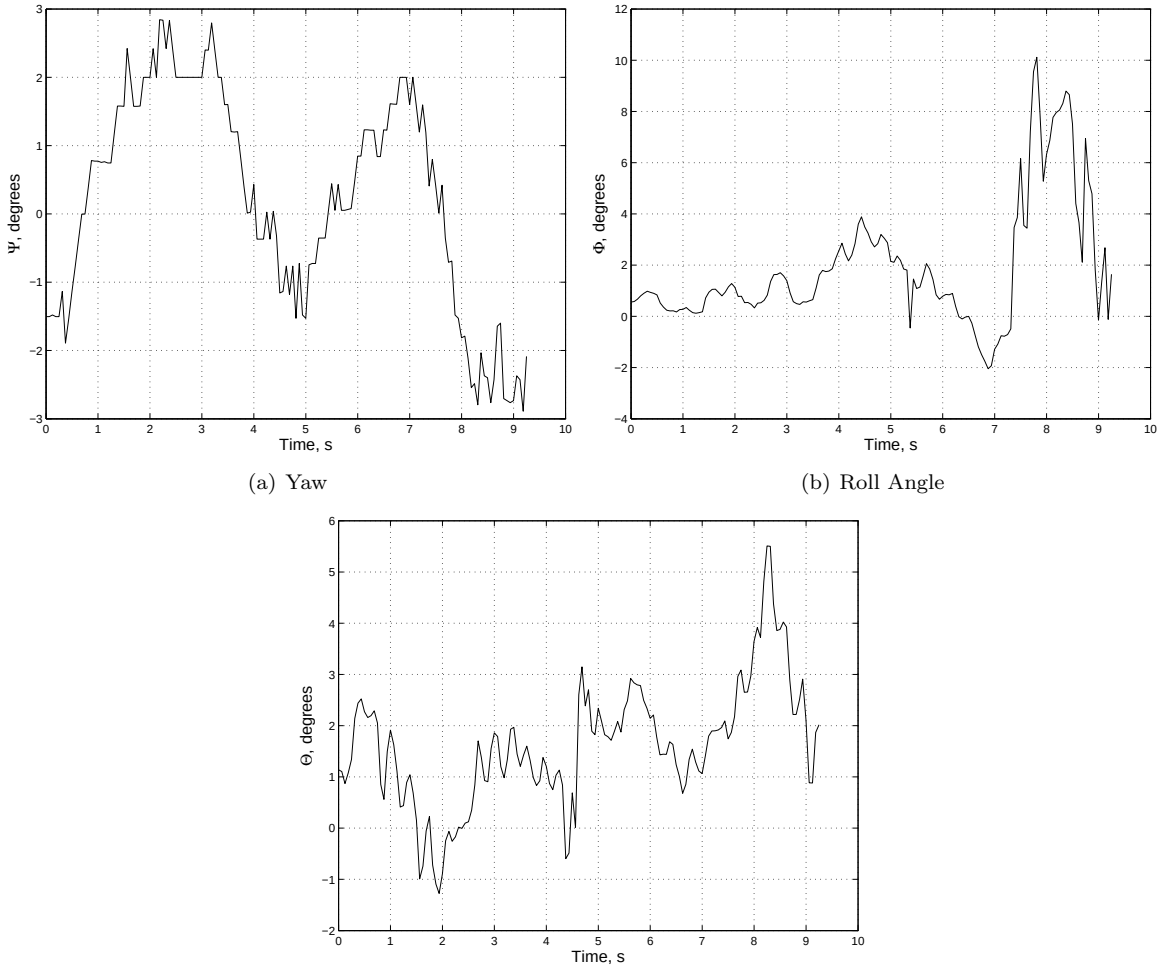

(a) Yaw

(b) Roll Angle

(c) Pitch Angle

Figure 16. Attitude flight data for quadrotor in hover condition.

VII. Conclusion

We have shown to ability to compute the 6 DOF estimation of a quadrotor vehicle and control it using the X,Y,Z, and yaw information based on moiré patterns. Having demonstrated the use of moiré patterns to hover, it can be extended to controlled movement within a space given the target remains in view. The target can also be utilized as a landing pad for the quadrotor vehicle given an artificial ground is created to ensure the red dots remain in the image plane at touchdown.

Embedded sets of varying sized printed gratings and feature points would enable vehicles to maneuver in larger spaces. Smaller sets within these patterns could be used with their associated feature points to guide vehicles downward once they have approached the target too closely to see the outlying feature points. Larger gratings would enable the vehicle to operate at higher altitudes since the patterns would remain discernable on the image plane and provide enough points for the DFT to be taken. Higher flying altitudes increase the X and Y operating area as well.

Applications of the moiré target are not limited to operations indoors. External landing platforms can greatly benefit from such a system by enabling piloted and autonomous vehicles alike to determine relative attitude and position to the landing surfaces with higher degrees of accuracy. Examples of such systems include the landing of rotorcraft on aircraft carrier decks, on moving ground vehicles, or in highly cluttered environments.

Acknowledgements

The authors would like to thank Brett Bethke, Michael Robbins, Erwan Salaun, Gaston Fiore, and Selcuk Bayraktar for their invaluable assistance in the project. This research has been generously supported by a fellowship from the MIT Department of Aeronautics and Astronautics, the Boeing-MIT Strategic Alliance, and by the Office Naval Research Grant N00014-03-1-0171.

References

[1]Saripalli, S., Montgomery, J. F., and Sukhatme, G. S., "Vision-based Autonomous Landing of an Unamnned Aerial Vehicle," *Proceedings of IEEE International Conference on Robotics and Automation*, IEEE, Wahington, DC, 2002, pp. 2799–2804.

[2]Feron, E. and Paduano, J., "A Passive Sensor for Position and Attitude Estimation Using an Interferometric Target," *IEEE Conference on Decision and Conrol*, Nassau, Bahamas, December 2004.

[3]Yang, Z. and Tsai, W., "Using Parallel Line Information for Vision-based Landmark Location Estimation and an Application to Automatic Helicopter Landing," *Robotics and Computer-Integrated Manufacturing*, Vol. 14, 1998, pp. 297–306.

[4]Altunğ, E., Ostrowski, J. P., and Taylor, C. J., "Quadrotor Control Using Dual Camera Visual Feedback," *Proceedings of IEEE International Conference on Robotics and Automation*, Taipei, Taiwan, September 2003.

[5]Wirin, W. B., "Real-time Attitude Estimation Techniques Applied to a Four Rotor Helicopter," *Proceedings of IEEE Conference on Decision and Control*, 2004, pp. 3980–3985.

[6]Sharp, C. S., Sahkernia, O., and Sastry, S. S., "A Vision System for Landing an Unmanned Aerial Vehcile," *IEEE Conference on Robotics and Automation*, 2001.

[7]O. Amidi and T. Kanade and K. Fujita, "A Visual Odometer for Autonomous Helicopter Flight," *Robotics and Autonomous Systems*, Vol. 28, 1999, pp. 1852–193.

[8]Vicon Peak, "Motion Capture Systems from Vicon Peak," http://www.vicon.com/products/systems.html, 2006.

[9]Metris, "Indoor GPS: Large Scale Metrology," http://www.indoorgps.com, 2006.

[10]E. Olsen, C.-W. P. and How, J. P., "3D Formation Flight using Differential Carrier-phase GPS Sensors," *Journal of the Institute of Navigation*, Vol. 1460, No. 1, 1999, pp. 35–48.

[11]Krumm, J. and Shafter, S. A., "Sampled-grating and Crossed-grating Models of Moire Patterns From Digital Imaging," *Optical Engineering*, Vol. 30, No. 2, 1991, pp. 195–206.

[12]Draganfly Innovations Inc., "Draganfly V Ti Pro Website," http://www.rctoys.com/draganflyer5tipro.php, January 2006.

[13]S. Bouabdallah, A. N. and Siegwart, R., "Modeling of the "OS" Quadrotor - Version 1.0," Tech. rep., Ecole Polytechnique Federale de Lausanne, 2004.

[14]Tournier, G. P., *Six Degree of Freedom Estimation Using Monocular Vision and Moiré Patterns*, Master's thesis, Massachusetts Institute of Technology, 2006.